Aerial Base Station Assisted Cellular Communication: Performance and Trade-Off

Navuday Sharma , Atul Kumar , Haris Pervaiz , Maurizio Magarini , Leila Musavian , Muhamamd Mahtab Alam , Anish Jindal, and Muhammad Ali Imran

Abstract—The use of Aerial Base Stations (ABSs) has received a great deal of attention in academia and industry as a means to support the cellular communication traffic growth. In this article, we focus on obtaining the optimal altitude of an ABS using two criteria - maximum cell coverage area and minimum Symbol Error Rate (SER). Our study is done by using a probabilistic air-to-ground channel model, developed for low altitude aerial platforms via simulations on a commercial ray tracing software, for different scenarios like Urban High Rise, Urban, and Suburban. The probability distributions of the received power of the ground users and of the power delay profile at optimal ABS altitude are provided as a function of the size of the cell area. For the SER analysis, we present a system model based on Generalized Frequency Division Multiplexing (GFDM), in a time-frequency grid that is compatible with Long Term Evolution, by implementing parameters for low latency communication at the physical layer. The impact of "Better than Nyquist" pulses on the GFDM system is evaluated in terms of SER performance. From the presented results, a significant improvement is demonstrated compared to the traditional Nyquist pulses.

Index Terms—Aerial base station, air-to-ground channel, generalized frequency division multiplexing (GFDM), optimal altitude, pulse shaping filters, symbol error rate (SER).

Navuday Sharma is with Ericsson Eesti AS, 11415 Tallinn, Estonia (e-mail: navuday.sharma@ericsson.com).

Atul Kumar is with Vodafone Chair Mobile Communications Systems, Technische Universitat Dresden, Dresden, Germany (e-mail: atul.kumar@tu-dresden.de).

Haris Pervaiz is with the School of Computing, and Communications (SCC), Lancaster University, Lancaster, Lancashire, U.K. (e-mail: h.b.pervaiz@lancaster.ac.uk).

Maurizio Magarini is with the Dipartimento di Elettronica, Informazione e Bioingegneria, Politecnico di Milano, Milano, Italy (e-mail: maurizio.magarini@polimi.it).

Leila Musavian and Anish Jindal are with the School of Computer Science, and Electronic Engineering, University of Essex, Colchester, Essex, U.K. (e-mail: leila.musavian@essex.ac.uk; a.jindal@essex.ac.ukSenior Member).

Muhamamd Mahtab Alam is with the Thomas Johann Seebeck Department of Electronics, Tallinn University of Technology, Tallinn, Estonia (e-mail: muhammad.alam@taltech.eeSenior Member).

Muhammad Ali Imran is with the School of Engineering, University of Glasgow, Glasgow, Glasgow, U.K. (e-mail: muhammad.imran@glasgow.ac.ukSenior Member).

Digital Object Identifier 10.1109/TNSE.2021.3052984

I. INTRODUCTION

THE unmanned aerial vehicles (UAVs[1]), commonly known as drones, have received a rapid proliferation in various applications due to their progress in payload capacity and prolonged battery life [2]. With initial development for military applications, such as surveillance and reconnaissance, UAVs have been also extended to civil sectors such as remote sensing, search and rescue, film making, weather detection, wildlife, agriculture monitoring and smart/secure lockdown monitoring in pandemic [3], [4]. Due to the recent advances in wireless communications, UAVs with low-cost transceivers mounted on board are envisioned to reform the paradigm of next generation networks [5], operating as low altitude aerial base stations (ABSs) and integrated with current cellular architecture [6], as shown in Fig. 1. An ABS can provide on-demand cellular coverage and enhanced data rates to the ground mobile users in a heterogeneous network (HetNet). In this regards, the third generation partnership group (3GPP) provided a technical report, entitled, "Enhanced LTE support for aerial vehicles" in September 2019 with four crucial requirements, as discussed with detail in [7]; listed as UAV traffic requirements; channel modeling to characterize air-to-ground (A2G) propagation; possibility to reuse the current LTE framework for aerial vehicles; and definition of enhancements in LTE Release 17 to assist UAV network. An overview of UAV-aided wireless communications, with three use cases: UAV-aided coverage, UAV-aided relaying, and UAV-aided information dissemination is provided in [8], [9]. Further, such architectures are optimized for enhancing the UAVs performance with respect to various quality-of-service (QoS) parameters such as UAV positioning, cellular coverage, energy optimization, cooperative communication, and routing protocols.

The ABS network architecture has a lot of research literature and experimental measurements available for channel characterization, power consumption analysis, placement and mobility optimization, fronthauling and backhauling etc. Here, we address the relevant literature on the aspects of UAV channel modeling, cellular coverage, and waveform analysis based on our motivation and contributions, provided later in this section. Many researchers have presented different methods to tackle some of these issues, as discussed in the following section.

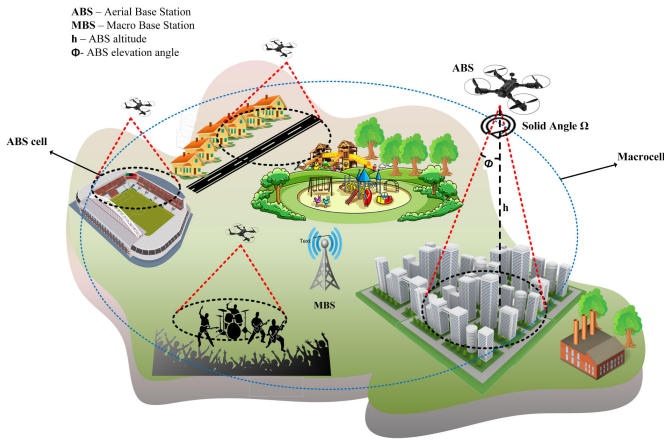[1] The term ABS and UAV are used interchangeably through out the article.

Fig. 1. Wireless cellular network architecture with integrated aerial base stations (ABSs).

A. Motivation

Despite the vast literature, to the best of our knowledge, there are no articles that consider the generalized waveforms and evaluate their impact on UAV-enabled communication to support low latency and high data rate requirements of ground mobile users, apart from our previous contribution in [1]. In the latter, the symbol-error-rate (SER) analysis was conducted for Generalized Frequency Division Multiplexing (GFDM) based A2G communication with variation of UAV altitude and "Better than Nyquist" (BTN) pulse shaping filters in urban high rise, urban, and suburban environments. In the present article, we further supplement our contribution by adding mobility to the UAV and obtaining an optimal UAV altitude under minimum SER. Also, we evaluate GFDM and OFDM SER for static and moving ABS under various Nyquist and BTN pulse shaping filters.

B. Relevant Works

A comprehensive survey on channel characterization and modeling for UAV communications, with deterministic and stochastic approaches and measurement campaigns, is provided in [10], as a low altitude aerial platform (LAP). The results of measurement campaigns are described for narrow and wide-band channel sounders, IEEE 802.11 transceivers, and cellular connected UAVs operating at either unlicensed frequency bands or respective bands, according to the considered technology. Furthermore, measurement results are shown for A2G and air-to-air (A2A) characterization with large scale parameters (LSP), such as path loss and shadowing, and small scale parameters (SSP), such as angular spread, delay spreads, and Ricean factor. With focus on similar aspects, reference [11] describes A2A and A2G aeronautical and UAV channel fading statistics, where aeronautical channels suggest the flight altitude of the aircraft is much higher as compared with that of the UAV considered as an LAP. Furthermore, classification of UAVs, timeline of civil aircrafts and UAV channel modeling campaigns are provided along with link budget, channel impulse response, antenna diversity, spatial

multiplexing, and multiple-input-multiple-output (MIMO) characteristics over rural, urban, and over the sea environments. Another relevant survey is [12], which describes in detail the impact of the Doppler effect and of the multipath channel propagation in different types of environments. Further, antenna configurations, channel sounding waveforms, effects of elevation angles are extensively elaborated. Since A2G and A2A channels are highly sensitive to line-of-sight (LoS) transmission, the elevation angle plays a significant role in defining the path loss dependence between the transmitter and the receiver. As the impact of elevation angle varies with the antenna directivity, in case of highly directional antennas, such as those used for communications at millimeter waves, the alignment of transmitter and receiver beams has negligible effect on communication for varying elevation angle. However, for omnidirectional or isotropic antennas the effect of the elevation angle can be significant [12], [13]. In [14], the ABS network employs both ultra-high frequency (UHF) and S-bands to provide connectivity to ground users, thus combining the advantages of small path loss in low frequency bands with that of large bandwidth in high frequency bands. Measurements results conducted in rural, suburban, and urban areas are shown with horizontal distance up to 70 Km from the airship and altitude up to 950 m. Similarly, [15] reports measurements carried out at 3.9 GHz in suburban environment with an omnidirectional antenna installed on a small UAV flying at an altitude of 40 m. The results of LSP and SSP from the measurements show reasonable agreement when compared with ray tracing simulations for the same scenario. There are several MIMO based UAV channel models, which can be found in [10]–[12]. However, UAV-MIMO channel is out of the scope of this paper.

The literature on UAV cellular coverage is broadly categorized into optimization of various parameters of architectures with single or multiple ABSs. However, there are limited contributions with respect to single ABS coverage. In [16], an analytical analysis is done to maximize the ABS coverage with an optimal altitude, which is a function of path loss and statistical parameters of the urban environment. An LoS path loss model is also derived from the ITU-R mathematical steps, which is used in this paper. In [17], the optimal UAV altitude to establish a reliable maximum coverage is addressed using A2G cooperative communication. Further under a specific scenario with low transmit power, an optimal altitude of 1300 m is shown without relaying, which varies between 700 m to 2000 m with relaying. In [18] the UAV flying altitude and the antenna beamwidth are jointly optimized for throughput maximization for downlink multicasting, broadcasting, and uplink multiple access multiuser communication models. Similarly, the joint optimization of UAV altitude, user association, and transmission direction to improve the system sumrate with prior knowledge of ground users' location is addressed in [19]. Also, there are many articles proposing an optimal deployment strategy of multiple UAVs' network to maximize the cellular coverage, with the constraints on downlink coverage probability, UAV placement, and minimum transmit power by each UAV. However, we do not refer to

those articles in the present paper since we analyze the parameters of a single ABS.

The research on PHY information transmission in ABS is limited. Reference [20], provides the candidate waveforms considering different operating requirements for UAV such as use of control and non-payload communication channel during high altitude cruise, taxing and take-off. Further, it also addresses constraints on UAV size, weight, and power. However, unlike this work, appropriate A2G channel models are not used and the UAV altitude is not taken into account by the authors, thereby discouraging the implementation of new waveforms for information transmission. Also in [21], the authors analyze the growth of UAV industry and spectrum requirements and discuss spectrum sharing as a possible solution to integrate the UAV network into the current cellular infrastructure. They use orthogonal frequency division multiplexing (OFDM) as the most suitable waveform. However, they only consider LoS A2G links in the channel model and ignore the multipath propagation effects, which are included in our simulation results in the range of the same UAV altitudes. In [22], the performance of an IEEE 802.11a compatible OFDM for UAV downlink with large Doppler shift and inter-carrier interference (ICI) is analyzed. Similarly, the effect of ICI and inter-symbol interference from multi-path propagation are analyzed in [23] for OFDM based UAV data link communication in urban environment. The fast Fourier transform (FFT) size of OFDM is increased to improve system performance with synchronization requirements. Realistic end-to-end ray tracing simulations are shown considering an A2G channel. In [24], an OFDM waveform design using software defined radio is considered.

As previously mentioned, only [1] describes the impact of adopting GFDM in UAV downlink transmission. However, GFDM has been researched for other use-cases and communication systems. In [25], the authors implement spread spectrum GFDM for integrated satellite-terrestrial communication and conduct performance analysis with SER and peak-to-average-power-ratio. Similar analysis is done with the same performance indicators and spectral efficiency in [26] for underwater acoustic channels considering different pulse shaping filters. Further, DC biased Optical GFDM has been proposed for visible light communication in [27] with performance analysis under double sided clipping. For improving the energy efficiency of internet-of-things (IOT) devices, radio resource allocation with wireless information and power transfer scheme has been addressed for multiuser GFDM system model in [28].

Apart from academic research, industrial experiments were performed by various companies to provide cellular and internet connectivity through aerial platforms. Qualcomm was able to demonstrate smooth handovers with zero link failures with autonomous drone control over LTE network [29]. Facebook Aquila project conducted successful flights with solar powered drones to provide internet connectivity in suburban areas at an altitude of $18 - 20$ Km with pre-defined waypoints to provide a cell coverage area of nearly 100 Km [30]. Aquila used free space optical links to ground access points which further

connected to mobile users using Wi-Fi or LTE technology. Also, Nokia worked on the project of "Connected UAVs" to implement a swarm and collision avoidance technology, which has multiple use cases in smart cities, transportation, search and rescue, etc [31].

C. Contributions

The main contributions of this paper are as follows:

- We compute an optimal altitude of the ABS for minimum SER and maximum ABS cell coverage in different environments. The optimal altitude is obtained from a static ABS by performing ray tracing simulations at different heights. However, the three dimensional propagation environment makes the channel results site-specific. We have eliminated this limitation by creating generalized environments, which are described in Section IV. Therefore, our results can be implemented for any realistic environments.

- We implement GFDM in our system model for ABS downlink performance analysis, as being considered the most suitable and compatible waveform for LTE, LTE-A, and LTE-Pro hybrid systems [32] due to its backward compatibility with the forth generation (4 G) frame structure. We use parameters of low latency communication (higher sub-carrier spacing and lower symbol duration) of physical layer (PHY) as given in Table III.

- We use A2G channel parameters for SER calculations in the GFDM model. We also provide the power delay profiles for A2G channel in different environments at the optimal altitude. For obtaining the A2G channel, similar ray tracing simulations were performed with static and moving ABS. Further, the distribution of the received power for ground receivers in different environments is also computed using the optimal ABS altitude, which supplements to find the variation of optimal altitude with cell radius.

- Finally, we implement various BTN pulse shaping filters in the GFDM transceiver to obtain SER at optimal ABS altitude and show significant performance gains as compared to Nyquist pulse shaping filters. These simulations were conducted for both static and moving ABS, to analyze the effect of Doppler shift on SER.

The rest of the article is organized as follows. In Section II, we address the GFDM system model for LAP A2G channel model. Section IV, describes the ray tracing simulation setup developed with various environmental and transceiver parameters. In Section V, we perform a trade-off analysis to obtain optimal ABS altitude for maximum cell coverage and minimum SER. We also provide the analytical expression of optimal altitude, the power delay profile, and the parameters of the received power distribution of ground users. Further, in Section VI we report various pulse shaping filters and present results to obtain the minimum SER in different environments. To the best of our knowledge, this article presents a unique study of performance analysis for ABS with different optimal

TABLE I
SUMMARY OF SYMBOLS AND THEIR DESCRIPTIONS

Symbols	Descriptions	Symbols	Descriptions
$\mathbf{d}$	Vector of high data-rate stream.	$\mathbf{h}$	Channel impulse response vector of size Sx1.
N	Total number of symbols.	$\mathbf{H}$	Circulant matrix of size SxS based on $\mathbf{h}$.
K	Total number of sub-carriers.	$\mathbf{w}$	Noise vector of size Sx1.
M	Total number of sub-symbols.	$\boldsymbol{y}_{eq}$	Equalized signal in time-domain.
$(\cdot)^T$	Transpose operator.	$\boldsymbol{B}_{MF}$	Modulator matrix of matched filter.
$d_{k,m}$	m^{th} complex sub-symbol transmitted on k^{th} sub-carrier of the block.	$\mathbf{A}$	Vector for pulse shaping filter.
T_s	Duration of the sub-symbol.	$\hat{d}$	Estimated data vector.
$g_{k,m}[n]$	Pulse shaping filter.	Δ	Roll-off factor of pulse shaping filter.
$g[n]$	Prototype filter.	$sech$	Hyperbolic secant function.
mod	modulo N operation.	$arcsech$	Inverse hyperbolic secant function.
N_{CP}	Length of the cyclic prefix.	h	Height of ABS.
η	Path loss exponent.	R	Radius of an area used for normalizing ABS cell area.
φ	Distance between ground receiver and ABS.	erf	Error function.
φ_0	Reference distance.	P_{th}	Received power threshold of ground users to maintain ABS link connectivity.
X_σ	Log-normal shadowing.	P_{TX}	Transmitted power by ABS.
σ	Standard deviation on log-normal shadowing.	G_T	Gain of ABS transmitting antenna.
PL_{LoS}	Path loss of line-of-sight link.	G_R	Gain of users receiving antenna.
PL_{NLoS}	Path loss of non-line-of-sight link.	PL_0	Reference path loss at distance r_0 from the ABS.
PL	Average Path loss from LoS and NLoS link.	Ω	Solid angle.
$\mathbb{P}_{\text{LoS}}$	Probability of LoS link.	$\mathbf{d}$	3D distance or the slant height formed from the geometry.
ω and ε	Parameters of the LoS curve from [16].	A	Cell area covered by ABS.
α, β and γ	Environment structuring variables as described in Sec. IV.	$\hat{n}$	Unit vector.
ϕ	Elevation angle between ABS and ground user.	θ	Azimuth angle between ABS and ground user.
$h[n]$	Channel impulse response.	P_{RX}	Received power by the ground user.
h_v	v^{th} complex Ricean fading coefficient.	P_{th}	Threshold of received power.
$\mathbf{x}$	Vector of transmitted signal.	$\mathbf{r}$	2D distance between the ABS and the user.

altitude determination criterion, which has not been addressed in the existing literature. The symbols and the notation used in this paper are addressed in Table I for quick reference.

II. SYSTEM MODEL

In the context of vehicular communication systems, both LTE vehicle-to-everything (V2X) [33] and the Wi-Fi based IEEE 802.11p [34] solutions implement OFDM modulation, which is characterized by high out-of-band (OOB) emission. In case of transmission over highly time and frequency selective fading channels, the performance of OFDM is severely impaired by channel estimation and synchronization errors. Therefore, OFDM may not be a desirable waveform for UAV communications in terms of inefficient usage of time and frequency resources [35]. Thus far, it is well known that GFDM is one of the multi-carrier schemes under consideration for the future networks architectures. Due to its low OOB emission obtained by circular pulse shaping filter, GFDM improves the spectral efficiency in short data burst transmission with ultra low latency scenario [32]. A characteristic of GFDM is that of being backward compatible with OFDM and single-carrier frequency division multiple access (SC-FDMA). Hence, we implement GFDM in our simulations. In the GFDM transmission scheme [36], the high data-rate stream in vector $\mathbf{d}$ contains N elements, which can be further decomposed into low symbol-rate streams of K sub-carriers with M sub-symbols each, by applying $\mathbf{d}$ to the GFDM modulator. As shown in
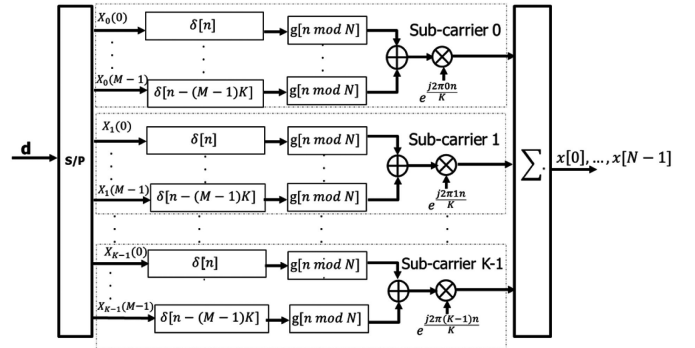

Fig. 2.   GFDM modulator block diagram [36].

Fig. 2, the input of the GFDM modulator is given by

$$\mathbf{d} = [\boldsymbol{d}_0, \, \mathbf{d}_1, \ldots, \mathbf{d}_{K-1}]^T,$$

where

$$\mathbf{d}_k = \left[d_{k,0}, \, d_{k,1}, .., d_{k,M-1} \right]^T,$$

with $(\cdot)^T$ being the transpose operator and $d_{k,m}$ the mth complex sub-symbol transmitted on k^{th} sub-carrier of the block. The total number of symbols is $N = KM$. The sub-carrier spacing is equal to $1/T_s$ and time-period of each data block $\mathbf{d}_k$ is MT_s, where T_s is sub-symbol duration.

The transmitted signal at the discrete-time index n is given by

TABLE II
RECEIVED POWER DELAY PROFILE WITH DELAY IN "NS" AND POWER IN "DB" AT OPTIMAL ALTITUDE FOR 10 TAP CHANNEL

Suburban scenario		Urban scenario		Urban High Rise scenario	
Delay	Power	Delay	Power	Delay	Power
2100	-66.44	1450	-23.51	2023	151.09
2530	-51.51	1496	14.35	2131	111.76
2595	25.67	1645	6.98	2324	80.49
2826	-19.77	1703	-56.25	2429	76.64
2836	-57.51	1752	-38.87	2732	92.23
3085	-31.31	1784	-71.12	2745	135.52
3390	22.59	1935	-56.66	2916	115.11
3463	28.87	2055	-41.83	3027	112.40
3870	-48.47	2191	-39.72	3105	82.96
3951	-34.55	2346	-63.87	3138	79.16

$$x[n] = \sum_{k=0}^{K-1} \sum_{m=0}^{M-1} d_{k,m} g_{k,m}[n], n = 0, 1, KM - 1, \quad (1)$$

where $g_{k,m}[n]$ is the corresponding pulse shaping filter

$$g_{k,m}[n] = g[(n - mK) \bmod N] e^{\frac{-j2\pi kn}{K}},$$

with $g[n]$ representing the prototype filter and mod denoting the modulo N operation, which makes $g_{k,m}[n]$ a circularly shifted version of $g_{k,0}[n]$. The exponential function performs the frequency shifting operation and n is the sampling index.

By collecting N samples of $g_{k,m}[n]$ in the matrix form, the vector representation of (1) can be written as

$$\mathbf{x} = \mathbf{A} \, \mathbf{d}, \quad (2)$$

where $\mathbf{x} = [x[0], x[1], \cdots, x[N-1]]^T$, and $\mathbf{A} = [\mathbf{g}_{0,0} \cdots \mathbf{g}_{K-1,0}. \mathbf{g}_{0,1} \ \mathbf{g}_{K-1,1} \ \mathbf{g}_{0,M-1}. \mathbf{g}_{K-1,M-1}]$.

Before transmitting over the A2G channel, the cyclic prefix (CP) of length N_{CP} is added to create the vector given as

$$\widehat{\boldsymbol{x}} = \left[\mathbf{x}(N - N_{CP} : N - 1)^T, \mathbf{x}^T \right]^T. \quad (3)$$

The CP length is taken equal as the number of taps in the channel for our simulations, *i.e*, 10 as reported in Table II.

Further, transmission with propagation effects such as path loss and large scale fading effects over A2G probabilistic channel [13] can be modeled as

$$\mathrm{PL}_{\mathrm{LoS}}(\varphi)[\mathrm{dB}] = 20 \log_{10}\left(\frac{4\pi\varphi_0}{\lambda}\right) + 10\eta_{\mathrm{LoS}} \log_{10}(\varphi) + X_{\sigma,\mathrm{LoS}}, \quad (4)$$

$$\mathrm{PL}_{\mathrm{NLoS}}(\varphi)[\mathrm{dB}] = 20 \log_{10}\left(\frac{4\pi\varphi_0}{\lambda}\right) + 10\eta_{\mathrm{NLoS}} \log_{10}(\varphi) + X_{\sigma,\mathrm{NLoS}}, \quad (5)$$

where LoS and NLoS denote line-of-sight and non-LoS, respectively, with η being the path loss exponent (PLE), PL representing the path loss, φ denoting the distance between ground receiver and ABS with φ_0 as the reference distance, assumed here as $\varphi_0 = 1$. X_σ represents the log-normal shadowing where σ is the standard deviation which includes the large scale fading effects. Thus far, the average PL model can be obtained as

$$\mathrm{PL}(\varphi)[\mathrm{dB}] = \mathbb{P}_{\mathrm{LoS}} \cdot \mathrm{PL}_{\mathrm{LoS}}(\varphi) + (1 - \mathbb{P}_{\mathrm{LoS}}) \cdot \mathrm{PL}_{\mathrm{NLoS}}(\varphi), \quad (6)$$

where $\mathbb{P}_{\mathrm{LoS}}$ is the LoS probability of the link [16] which is modeled as

$$\mathbb{P}_{\mathrm{LoS}} = \frac{1}{1 + \omega \exp(-\varepsilon[\phi - \omega])}, \quad (7)$$

being ω and ε the parameters of the LoS curve, depending on the environment structuring variables, α, β and γ as given in Sec. IV and ϕ being the elevation angle between the ABS and the ground user, depending on the type of antenna used as shown in Fig. 1. The channel parameters such as PL and X_σ in different environments and UAV altitudes were obtained from ray tracing simulations, as will be explained in Section IV. However, this model does not include the small scale fading effects.

The coefficients of the discrete-time channel impulse response $h[n]$ are usually modeled as Ricean for A2G channel [37]. In fact, $h[n]$ can be derived via stochastic methods through empirical data, simulations, and geometric analysis [37]. Here, we implement the map-based approach to obtain the data and model $h[n]$ as

$$h[n] = \sum_{\upsilon=0}^{\Pi-1} h_\upsilon \delta[n - \upsilon], \quad (8)$$

where $\delta[n]$ is the Kronecker delta and h_υ is the υth complex Ricean fading coefficient, which is evaluated via ray tracing channel propagation data as $\mathrm{PG} = -(\mathrm{PL}_{\mathrm{tot}}(\varphi)[\mathrm{dB}] - (\mathbb{P}_{\mathrm{LoS}} \cdot \mathrm{PL}_{\mathrm{LoS}}(\varphi) + (1 - \mathbb{P}_{\mathrm{LoS}}) \cdot \mathrm{PL}_{\mathrm{NLoS}}(\varphi)))$ and Π represents the number of channel taps. PG denotes the channel power gain for each channel tap and $\mathrm{PL}_{\mathrm{tot}}(\varphi)[\mathrm{dB}]$ shows the total PL including both shadowing and multipath fading effects. At the GFDM receiver, we scrutinize the CP length should be greater than the maximum delay spread of the A2G channel, i.e, $N_{CP} \geq \Pi$. Under such presumption and after removing the CP, the received signal vector can be written as

$$\mathbf{y} = \mathbf{H}\mathbf{x} + \mathbf{w}, \quad (9)$$

where $\mathbf{H}$ denotes the circulant matrix of size $N \times N$ based on $\mathbf{h}$, which is $(N \times 1)$ vector where first Π elements represent channel impulse response and the remaining $N - \Pi$ are null. Further, $\mathbf{w}$ represents the noise vector of size $N \times 1$ where every element is an independent and identically distributed Gaussian random variable with zero mean and variance σ_w^2. Under the consideration of Matched Filter (MF); the equalized signal in time domain using the modulator matrix $\mathbf{B}_{MF} = (\mathbf{A}^H \mathbf{A})^{-1} \mathbf{A}^H$, the estimated data vector is

$$\hat{\mathbf{d}} = \mathbf{B}_{MF} \mathbf{y}_{eq} = \mathbf{B}_{MF} \mathbf{A}\mathbf{d} + \mathbf{B}_{MF} \mathbf{H}^{-1} \mathbf{w} \quad (10)$$

where $\mathbf{y}_{eq}$ is the equalized signal in time-domain and MF receiver maximizes the Signal to Noise-Ratio (SNR) per sub-carrier.
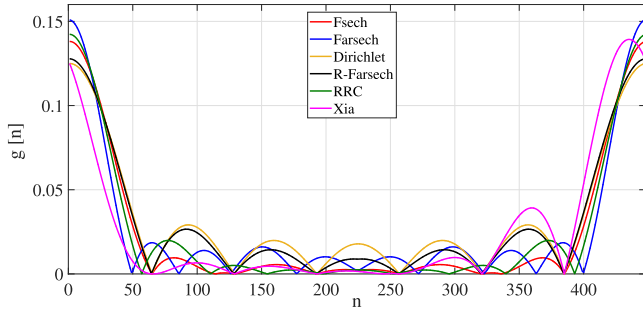
Fig. 3. Frequency response of the employed pulse shaping filters.

The spectral efficiency of the GFDM system is affected by the pulse shaping filter $g[n]$. Thus, we use BTN pulse shaping filters as reported in [38] and shown in Fig. 3. A standard approach for choosing the pulse shaping filter is to sample a continuous-time impulse response $g(t)$ windowed as

$$g_w(t) = \begin{cases} g_{wdown}(t), & 1 \leq t \leq KT_s, \\ g_{wup}(t), & (MK-K)Ts \leq t \leq (MK)T_s, \\ 0, & \text{otherwise,} \end{cases} \quad (11)$$

where $g_{wup}(t) = g_{pulse}(t)$, $g_{wdown}(t) = 1 - g_{pulse}(t)$ and T_s symbol interval, being $g_{pulse}(t)$ one of the different types of pulse shaping filters reported below.

To evaluate the performance of our system, we will address a trade-off analysis in Section V to obtain the optimal altitude of the UAV. This will be based on the maximum cellular coverage with A2G probabilistic channel parameters obtained via ray tracing simulations in Section IV and minimum SER with GFDM transmission scheme. Moreover, to address the impact on the SER performance of different BTN pulse shaping filters, in Section III we will show their time-domain expressions and in Section VI we will evaluate the performance by means of computer simulations.

III. PULSE SHAPING FILTER

In this section, the pulse shaping filters used for performance assessment of the GFDM system model are addressed. Their time-domain expressions are given in the sub-sections that follows.

A. Root Raised Cosine (RRC)

For the given roll-off factor Δ, the time domain equation of the root raised cosine (RRC) filter is given as

$$g_{RRC}(t) = \sqrt{g_{RC}(t)}. \quad (12)$$

where

$$g_{RC}(t) = \begin{cases} 1, & |t| \leq \frac{(1-\Delta)T_s}{2}, \\ \frac{1}{2}[1+\cos(\pi Q_{RC}(t))], & \frac{(1-\Delta)T_s}{2} < |t| \leq \frac{(1+\Delta)T_s}{2}, \\ 0, & \text{otherwise,} \end{cases}$$

$$\quad (13)$$

where $Q_{RC}(t)$ is the inner argument of $\cos$, as given in [39].

B. Flipped-Hyperbolic Secant (Fsech)

As proposed in [38], we implement the BTN pulse shaping filter, $Fsech$, which is defined as

$$g(t) = \begin{cases} 1, & |t| \leq \frac{(1-\Delta)T_s}{2}, \\ 1-sech(\rho P_{1\,Fsech}(t)), & \frac{(1-\Delta)T_s}{2} < |t| \leq \frac{T_s}{2}, \\ sech(\rho P_{2\,Fsech}(t)), & \frac{T_s}{2} < |t| \leq \frac{(1+\Delta)T_s}{2}, \\ 0, & \frac{(1+\Delta)T_s}{2} < |t|, \end{cases} \quad (14)$$

where $sech$ being the hyperbolic secant function, $\rho = ln(\sqrt{3}+2)/\Delta \times \frac{T_s}{2}$, $P_{1\,Fsech}(t)$ and $P_{2\,Fsech}(t)$ are the inner arguments of $sech$ as provided in [39].

C. Flipped-Inverse Hyperbolic Secant (Farcsech)

Furthermore, as proposed in [38], another implemented BTN pulse shaping filter is $Farcsech$, which is defined as

$$g(t) = \begin{cases} 1, & |t| \leq \frac{(1-\Delta)T_s}{2}, \\ arcsech\left(\frac{1}{\rho} P_{1\,Farcsech}(t)\right), & \frac{(1-\Delta)T_s}{2} < |t| \leq \frac{T_s}{2}, \\ 1-arcsech\left(\frac{1}{\rho} P_{2\,Fsech}(t)\right), & \frac{T_s}{2} < |t| \leq \frac{(1+\Delta)T_s}{2} \\ 0, & \frac{(1+\Delta)T_s}{2} < |t|, \end{cases}$$

$$\quad (15)$$

where $arcsech$ represents the inverse $sech$ function, $P_{1\,Farcsech}(t)$ and $P_{2\,Fsech}(t)$ are the inner arguments of $arcsech$ as provided in [39].

IV. RAY TRACING SIMULATION SETUP

The customized simulation setup was created to obtain the attributes of LAPs' A2G channel model with different ABS transmitting powers and altitudes. We develop three environments, i.e. Urban High Rise, Urban, and Suburban, on 3DS MAX, a Computer-Aided-Design (CAD) software, according to the parameters provided by ITU-R [40]:

- α = Proportion of field area covered by the infrastructure to the total area (dimensionless).
- β = Average number of buildings per unit area (building/ sq km).
- γ = Variable to address the height distribution of the buildings. A Rayleigh distribution is proposed by ITU-R.

The values of α, β and γ along with other city layout parameters, such as number of buildings, street width, building size, and material, are given in [13]. The CAD environments were of area 2000×2000 m ^{2}, from which ray tracing was done over 1000×1000 m^2 at various points. Two set of simulations were performed - moving and static ABSs. For static ABS, it was presented at the center of the snapshot, with approximately 33000 receivers spread uniformly over the entire surface of the environment with 5 m spacing from each other. There were no receivers inside buildings, since outdoor propagation was studied to support flash crowds. For moving ABS, a circular trajectory of ABS was considered, as shown in Fig. 4. The buildings' height and density were most in
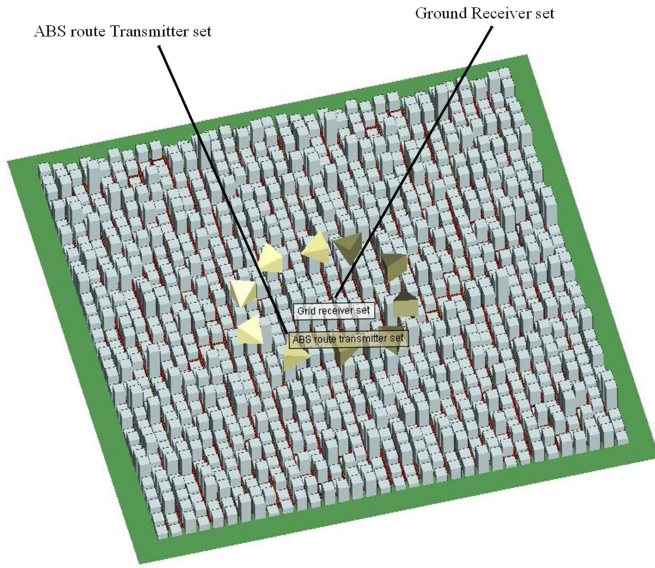
Fig. 4.   Urban High Rise Scenario with moving ABS altitude of 600 m in Wireless InSite.

Urban High Rise environment and least in the Suburban. Also, conventional earth materials and concrete were implemented for terrain and buildings, respectively. The ray tracing simulation was conducted in Wireless InSite 3.0.1 [41], a commercial software radio wave propagation. The accuracy of practical measurements from the software is well defined in [42]. The simulations were performed in the 2.4 GHz unlicensed band with 20 MHz bandwidth for UAV heights up to 2000 m altitude, with step of 100 m, and transmission power in the range from 18 to 46 dBm, at every 2 dBm interval. The simulations were conducted in sub-6 GHz as it was preferred in 3GPP [7], where many field trials were conducted by industries. The unlicensed spectrum of LTE was adopted due to unavailability of dedicated spectrum for such ABS architecture. The average of results from various snapshots at each UAV height were taken to improve the accuracy of the results. The receivers outside the buildings were only considered for the simulation. Figure 4 shows a snapshot of the simulation in Urban High Rise environment. Further, Table II, refers to the received power delay profile of ground user at optimal altitude of the ABS. The antenna on the UAV was taken to be isotropic with 2 dB gain to remove directivity effects on the A2G channel measurements.

## V. TRADE-OFF ANALYSIS FOR OPTIMAL ALTITUDE OF ABS

In this section, we obtain the optimum altitude of an ABS by focusing on two different parameters - minimum SER and maximum ABS cell coverage area. For obtaining the SER, we use a flexible multi-carrier modulation scheme, GFDM, where the sub-carriers are individually pulse-shaped in a block structure of K sub-carriers and M sub-symbols.

A. Optimal Altitude for Maximum Cell Coverage by ABS

Here, we derive a closed-form expression for the optimal altitude of the ABS. The variation of the cell coverage with
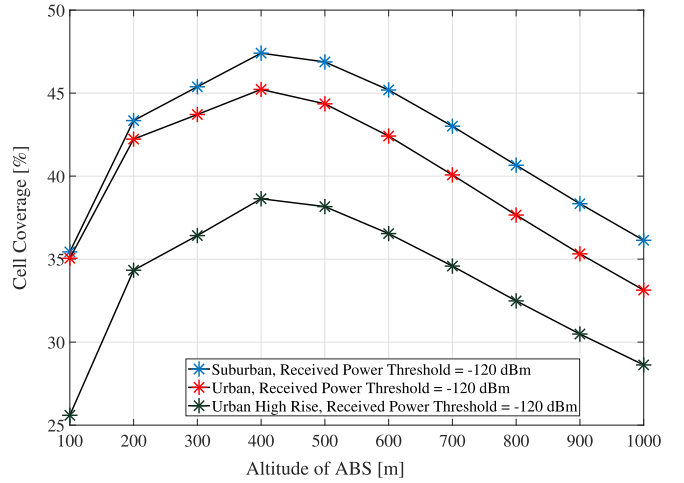
(a) Cell coverage variation with altitude of ABS.
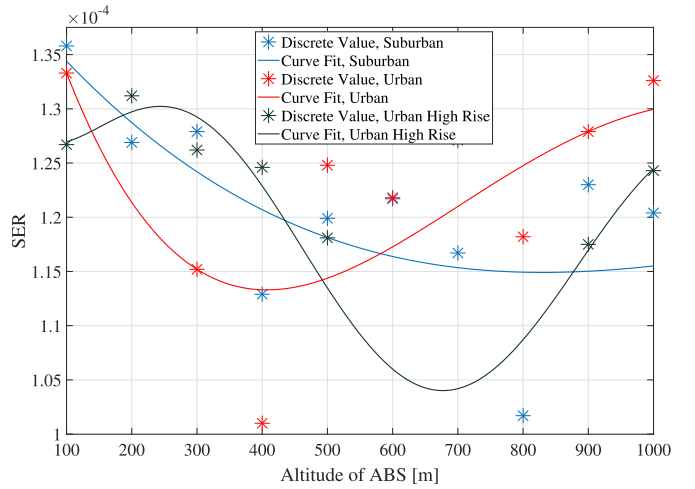
(b) SER variation with altitude of ABS.

Fig. 5.   Trade-off between maximum cell coverage and minimum SER to obtain optimal altitude. (a) [Cell coverage variation with altitude of ABS.] (b) [SER variation with altitude of ABS.]

height of ABS is given in Fig. 5(a), where $300 - 400$ m was observed as an optimal altitude for the same ray tracing simulations, in different environments. Reference [43] considers a generic received power threshold approach, where the cell coverage depends on the distance between the ABS and ground users receiving power, greater than the threshold required to maintain connectivity with the ABS. However, such an approach is implementable for any power source to define its boundaries. Therefore, we report a novel equation using a solid angle approach, taking into account A2G channel, antenna characteristics, ABS altitude, transmission power, and elevation angle with respect to users.

Lemma 1: The expression of cell area covered by an ABS is given by

$$A = \frac{2 \, h^2}{R} \left(\sec(\phi_{max}) - 1 \right)$$
$$\left[\left(\frac{1 - erf(a)}{2} \right) - \frac{1}{2} \exp\left(\frac{1 - 4ab}{4b^2} \right) \left[erf\left(\frac{1}{2b} - a \right) - 1 \right] \right],$$
$$\tag{16}$$

where h is the height of ABS, R is the radius of an area used for normalizing ABS cell area, erf is the error function, a and b are substitution parameters, given as

$$a = \frac{1}{\sigma\sqrt{2}}(P_{th}[dB] - P_{TX}[dB] - G_T[dB] - G_R[dB]$$
$$+ \text{PL}_0[dB] + 10\eta \log_{10}(R/r_0)), \tag{17}$$

$$b = \frac{10\eta \log_{10}(e)}{\sigma\sqrt{2}}, \tag{18}$$

with P_{th} is the received power threshold of ground users to maintain ABS link connectivity, P_{TX} is the transmitted power by ABS, G_T and G_R are the transmitting and receiving antenna gains, respectively, PL is further written as a function of reference path loss PL_0, at distance r_0 from the transmitter, as per close-in reference distance path loss model [44].

Proof: In order to obtain (16) we utilize a solid angle approach, where solid angle (Ω) [45] is a 3D analogue of an angle, enclosed by a conical surface at the apex as shown in Fig. 1. The solid angle subtended by an element on the ground at ABS is given by

$$d\Omega = \frac{d\vec{A}}{\mathbf{d}^2} \cdot \hat{n}, \tag{19}$$

where $\mathbf{d}$ is the 3D distance or the slant height of the cone formed from the geometry and $\hat{n}$ is the unit vector from the origin. From (19) we have $dA = \sin\phi\, \mathbf{d}^2\, d\theta\, d\phi$, where $d\theta$ and $d\phi$ are azimuth and elevation angles, respectively. This relationship is only based on geometrical aspects. Therefore, the probability parameter $\mathbb{P}(P_{RX}(\mathbf{r}) \geq P_{th})$ is added to the above expression. This produces the actual coverage by the ABS. This parameter denotes the probability that the received power by the ground user $P_{RX}(\mathbf{r})$ is greater than P_{th} and $\mathbf{r}$ is the 2D distance between the ABS and the user. Thus, we have

$$dA = \sin\phi\, \mathbf{d}^2\, \mathbb{P}(P_{RX}(\mathbf{r}) \geq P_{th})\, d\theta\, d\phi\, dr. \tag{20}$$

Thereby, integrating (20) under respective integral limits for minimum and maximum of each variable and normalizing the cell coverage, we have

$$A = \frac{\mathbf{d}^2}{A_C} \int_{\phi=0}^{\phi=\phi_{max}} \sin\phi\, d\phi \int_{\theta=0}^{\theta=2\pi} d\theta \int_0^R \mathbb{P}(P_{RX}(\mathbf{r}) \geq P_{th})dr, \tag{21}$$

where R corresponds to ϕ_{max}. $A_C = \pi R^2$ is the cell area used to normalize the final cell coverage A. Thus, from (21) we have

$$A = \frac{2\pi h^2}{A_C} \int_{\phi=0}^{\phi=\phi_{max}} \frac{\sin\phi}{\cos^2\phi}\, d\phi \int_0^R \mathbb{P}(P_{RX}(\mathbf{r}) \geq P_{th})dr.$$

Now integration of each part is shown separately as

$$A = \frac{2\pi h^2}{A_C} I_1 I_2 \tag{22}$$

where

$$I_1 = \int_{\phi=0}^{\phi=\phi_{max}} \frac{\sin\phi}{\cos^2\phi}\, d\phi = \sec(\phi_{max}) - 1 \tag{23}$$

and

$$I_2 = \int_0^R \mathbb{P}(P_{RX}(\mathbf{r}) \geq P_{th})dr. \tag{24}$$

The term I_2 can be calculated using Q-function as $\mathbb{P}(P_{RX}(\mathbf{r}) \geq P_{th}) = Q(\frac{P_{th}-\overline{P}_{RX}(\mathbf{r})}{\sigma})$. The Q-function is defined in the form of error function as

$$Q(x) = \int_x^\infty \frac{1}{\sqrt{2\pi}} \exp\left(-\frac{y^2}{2}\right) dy = \frac{1}{2}\left[1 - erf\left(\frac{x}{\sqrt{2}}\right)\right].$$

By replacing x with $(\frac{P_{th}-\overline{P}_{RX}(\mathbf{r})}{\sigma})$,

$$Q\left(\frac{P_{th} - \overline{P}_{RX}(\mathbf{r})}{\sigma}\right) = \frac{1}{2}\left[1 - erf\left(\frac{P_{th} - \overline{P}_{RX}(\mathbf{r})}{\sqrt{2}\sigma}\right)\right].$$

By further substitution with log-distance path loss model (in dB), $\overline{P}_{RX}(r) = P_{TX} + G_T + G_R - PL$, and by substituting for PL, we have,

$$\overline{P}_{RX}(r) = P_{TX} + G_T + G_R - \left(PL_0 + 10\eta \log_{10}\left(\frac{r}{r_0}\right)\right),$$

where P_{TX} is the transmitted power, G_T and G_R are the transmitting and receiving antenna gain, respectively, PL is the path loss which is further written as a function of reference path loss PL_0, at distance r_0 from the transmitter, and path loss exponent η. Therefore, we have

$$\mathbb{P}(P_{RX}(r) \geq P_{th}) = \frac{1}{2}\left[1 - erf\right.$$
$$\left.\left(\frac{P_{th} - [P_{TX} + G_T + G_R - [PL_0 + 10\eta \log_{10}(\frac{r}{r_0})]]}{\sigma\sqrt{2}}\right)\right],$$

where we substitute the following for clarity

$$a = \left(\frac{P_{th} - P_{TX} - G_T - G_R + PL_0 + 10\, ta\log_{10}(R/r_0)}{\sigma\sqrt{2}}\right)$$

and

$$b = \frac{10\eta\log_{10}(e)}{\sigma\sqrt{2}}.$$

Therefore, we represent

$$\mathbb{P}(P_{RX}(r) \geq P_{th}) = \frac{1}{2} - \frac{1}{2}erf\left(a + b\ln\frac{r}{R}\right)$$

and

$$I_2 = \int_0^R \mathbb{P}(P_{RX}(r) \geq P_{th})dr$$
$$= \int_0^R \frac{1}{2} - \frac{1}{2}erf\left(a + b\ln\frac{r}{R}\right)dr. \tag{25}$$

TABLE III
PARAMETERS FOR GFDM SIMULATION WITH LTE GRID [32]

Parameter	Normal mode
Subframe duration	1 ms or 30.720 samples
GFDM symbol duration	66.67 μs or 2048 samples
Subsymbol duration	4.17 μs or 128 samples
Subcarrier spacing	240 KHz
Subcarrier bandwidth	240 KHz
Sampling freq. (clock)	30.72 MHz
Subcarrier spacing factor N	128
Subsymbol spacing K	128
active subcarriers N_{on}	75
Subsymbols per GFDM symbol M	15
GFDM symbols per subframe	15
CP length	4.17 μs or 128 samples

Replacing $t = a + b \ln \frac{r}{R}$

$$I_2 = \frac{R}{2} - \frac{R}{2b} \int_{-\infty}^{a} \exp\left(\frac{t-a}{b}\right) erf(t) dt.$$

Integrating by parts, we obtain

$$I_2 = R\left[\left(\frac{1 - erf(a)}{2}\right) - \frac{1}{2}\exp\left(\frac{1 - 4ab}{4b^2}\right)\right.$$
$$\left.\left[erf\left(\frac{1}{2b} - a\right) - 1\right]\right].$$

Now substituting for I_1, I_2 and A_C in (22), we finally get (16). From (22), the optimal height of ABS for maximum coverage can be obtained as $\frac{dA}{dh} = 0$. Therefore,

$$h = \frac{R^2}{4 I_1 I_2} \tag{26}$$

$$h = \frac{R}{4(\sec(\phi_{max}) - 1)\left[\left(\frac{1-erf(a)}{2}\right) - \frac{1}{2}\exp\left(\frac{1-4ab}{4b^2}\right)\left[erf\left(\frac{1}{2b} - a\right) - 1\right]\right]} \tag{27}$$

By implementing the parameters of simulations as given in [43], the curves of cell coverage with respect to ABS altitude from (16) were found to be similar. Therefore, we acknowledge $300 - 400$ m as the optimal altitude of ABS in different environments as shown in Fig 5 (a).

Remark 1: From (26), I_1 and I_2 cannot be equal to zero, for the equation to hold. Therefore, analytically from (23), $\sec \phi_{max} - 1 \neq 0 \Rightarrow \phi_{max} \neq \frac{n\pi}{2}$, where $n \subset \mathbb{Z}$ (set of integer values) and since ϕ is the elevation angle, $\max(\phi) = \frac{\pi}{2}$. Also from (24),

$$\mathbb{P}(P_{RX}(\mathbf{r}) \geq P_{th}) = Q(\frac{P_{th} - \overline{P}_{RX}(\mathbf{r})}{\sigma}) \neq 0.$$

$\Rightarrow (\frac{P_{th} - \overline{P}_{RX}(\mathbf{r})}{\sigma}) \leq 3$ or $P_{th} \leq 3\sigma + P_{RX}$, since $\lim_{x \geq 3} Q(x) \to 0$. Therefore, the threshold received power should not be greater than received power by three times the standard deviation of log-normal shadowing for (26) to be valid.
Remark 2: For mobile operators to use ABS network, they have to tune the parameters such as P_{th}, P_{TX}, G_T and G_R depending on the SER, height and ABS cell coverage required. From Fig. 5 (a) and (b), we can infer that at the

desired value of SER, SER_{th}, a corresponding ABS altitude h_{th} can be obtained, depending on the type of environment and waveform used for transceiver. Therefore, a geometrical coverage area A' can be obtained excluding channel propagation effects as

$$A' = \pi R'^2 = \pi(h_{th} \tan(\phi_{max}))^2$$

where R' is the radius of ABS cell coverage. From (16), A can be replaced by A', and reorganized as follows

$$\frac{A'R}{2\,h^2(\sec(\phi_{max}) - 1)} = \left[\left(\frac{1 - erf(a)}{2}\right)\right.$$
$$\left. - \frac{1}{2}\exp\left(\frac{1 - 4ab}{4b^2}\right)\left[erf\left(\frac{1}{2b} - a\right) - 1\right]\right] \tag{28}$$

It is important to mention from (17) and (18), if $c = \frac{1}{\sqrt{2}}(10\eta \log_{10}(e) - 10\eta \log_{10}(\frac{R}{r_0}))$ from **Lemma 1**, it will imply that $a = b$, where $c = \frac{P_{th} - P_{TX} - G_T - G_R + PL_0}{\sqrt{2}}$. Also, for special case $R = e \times r_0$, b from (18) can be rewritten in the form of a defined in (17) as

$$b = a - \frac{c}{\sigma}. \tag{29}$$

Therefore, (28) can be rewritten as

$$F(a) - Y = 0, \tag{30}$$

where F(a) can be obtained by substituting b from (29) into Right Hand Side (RHS) of (28) and $Y = \frac{A'R}{2\,h^2(\sec\phi_{max} - 1)}$. We can easily find the root of (30), which will give us the value of a. The channel parameters such as η and σ can be obtained at different altitudes from [13]. ∎

B. Optimal Altitude for Minimum SER by ABS

In order to obtain the optimal altitude for the minimum SER, a GFDM transceiver system on an LTE grid was implemented by considering a low latency scenario. The parameters of the simulation have been taken from [32], and are provided in Table III. Reference [32] also describes the implementation of GFDM for a low latency scenario, where the main approach is to reduce the GFDM symbol duration and add a single cyclic prefix for the M sub-symbols. Here, the GFDM symbol duration was kept to 1 ms subframe duration. Based on these parameters, SER simulations were carried out for Suburban, Urban, and Urban High Rise environments to obtain optimal ABS altitude, with different power delay profiles at different altitudes. These profiles were obtained from ray tracing simulations for probabilistic A2G LoS channel model. We consider a Ricean fading model since LoS probability increases with increase in ABS altitude [16]. In Fig. 5(b), we plot the SER versus the ABS altitude for the considered environments as discrete values and obtain a curve fit to show the variation. We observe less variation of SER with altitude for Suburban scenario as compared to Urban and Urban High rise scenarios, which is probably due to the higher LoS probability in Suburban than Urban and Urban High Rise [16]. This implies that

TABLE IV
PROBABILITY DISTRIBUTION PARAMETERS OF RECEIVED POWER AT OPTIMAL ALTITUDE

Environment	Optimal Altitude [m]	Distribution type	Distribution parameters			
			μ (location)	σ (scale)	ν (degrees of freedom)	k (shape)
Suburban	600	t location-scale	−94.9520	2.5348	1.7666	-
Urban	400	Extreme Value	−75.7450	6.0756	-	-
Urban High Rise	600	Generalized Extreme Value	−95.5724	15.5478	-	−0.5446

the ground users would receive an LoS ray component of the Ricean channel with higher probability, which also increases with the ABS altitude, thereby producing lower variation in SER with ABS height. Conversely, in Urban and Urban High Rise scenarios, the SER variation is high due to low LoS probability, which tend to increase the effect of scattered components of multipath. Also the range in y-axis is limited in Fig. 5 (b) due to the frequency-flat fading scenario observed for ABS. As can be seen from Fig. 5(b), the optimal altitude for minimum SER is as follows: Suburban - 800 m, Urban - 400 m and Urban high Rise - 800 m.

C. Optimal Altitude With Varying Cell Radius for Different Received Power Thresholds

As observed in Sections V-A and V-B, the optimal altitude of ABS has to be a trade-off for maximum coverage and minimum SER which we report in Table IV. In this section we address the probability distributions of the received power of ground users at optimal altitude of ABS, which are given in Fig. 6. The received power has been obtained from ray tracing simulations as described in Section IV. The received power was fitted with several probability distributions such as Normal, Nakagami, Rayleigh, Ricean, Exponential, Beta, Birnbaum-Saunders, Extreme value, Generalized extreme value, Gamma, t location-scale, Weibull, Logistic, Gaussian etc. From all these distributions the closest and best fit distribution is shown in Fig. 6. The parameters of the distributions are provided in Table IV. With such parameters, the received power can be extracted as random values without performing ray tracing simulations or practical measurements. These values were used to obtain the variation of optimal ABS altitude h with respect to cell radius R for all considered environments as shown in Fig. 7. The behavior of the curves expects to follow (27), where h depends on R and substitution parameter a, which also depends on R. However, [16] shows a linear variation of the optimal LAP altitude with the radius of the cell when constrained on maximum allowed path loss, which is the threshold value for maintaining the link connectivity. This is different from our approach since we consider minimum SER and maximum cell coverage constraints for obtaining optimal altitude. Here, we also show the variation with received power threshold of ground users. We observe, for higher thresholds, a high optimal altitude is required to cover the same cell radius with minimum SER. Also, the optimal altitudes for Suburban and Urban High Rise are higher than Urban, as shown in Fig. 7 and Table IV.

In this section, the considered trade-off is between ABS cellular coverage and SER in GFDM transmission, as the fundamental key performance indicators of our system model. However, to improve it further, more complex optimization problems can be developed by including other parameters, which are described as a part of our future work in Section VII.

VI. PERFORMANCE EVALUATION WITH "BETTER THAN NYQUIST" PULSE SHAPING FILTERS

The choice of pulse shaping filters strongly affect the spectral properties of a signal. The most commonly used Nyquist pulse is raised cosine pulse. Here, we have implemented BTN pulses such as Flipped-hyperbolic secant (Fsech), Flipped-inverse hyperbolic secant (Farcsech) and Reverse-Farcsech (R-Farcsech) pulse shaping filters which enables GFDM to achieve better SER performance as compared to raised-cosine pulse [39]. These filters were proposed in [46] to improve sensitivity to timing jitter in the context of single-carrier modulation. We compare results of these filters with Root-raised cosine and Xia pulses.

Figure 8 shows the SER analysis using the BTN filters for the three considered environments at optimal altitude of static ABS. We use the power delay profile given in Table II and Ricean factors given in [13], as A2G channel parameters for this simulation. We observe that ABS downlink at 2.4 GHz frequency band, follows a frequency-flat fading channel. Also, SER was found to be lower for all SNR values, for ABS downlink communication as compared to terrestrial one [38]. From Fig. 8, we also observe that SER is higher for Suburban environment, lower for Urban and least for Urban High Rise environment, for optimal altitude. This can also be addressed from Fig. 5(b). This is probably due to higher optimal altitude in Suburban scenario than Urban environments, chosen according to two different criterion as mentioned in previous sections. Therefore, this addresses for an effective use of ABS in Urban environments. We also address the results with moving ABS with maximum Doppler shift of 3704 Hz, as shown in Fig. 10, which implies the ABS is cruising with very high speed relative to the ground users. With such fast mobility, the coherence time of the multipath channel is expected to decrease and Doppler shift to increase. However, we did not observe large variations in moving ABS as compared to static ABS due to frequency-flat fading scenario, although SER values were found to be higher. Further, we implement a circular trajectory of the ABS to achieve uniformity in its motion, to eradicate any possible inaccuracy in the received power of the ground users in ray tracing simulations due to sharp trajectory deviations. Also, homogeneity of ITU-R specified environments ensure the certainty of the results.
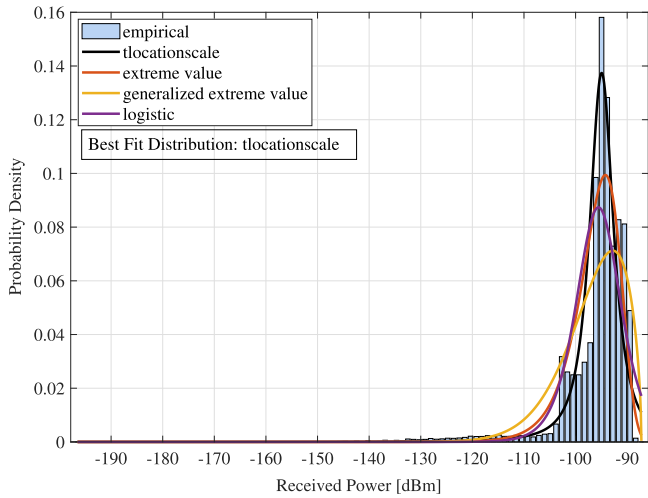
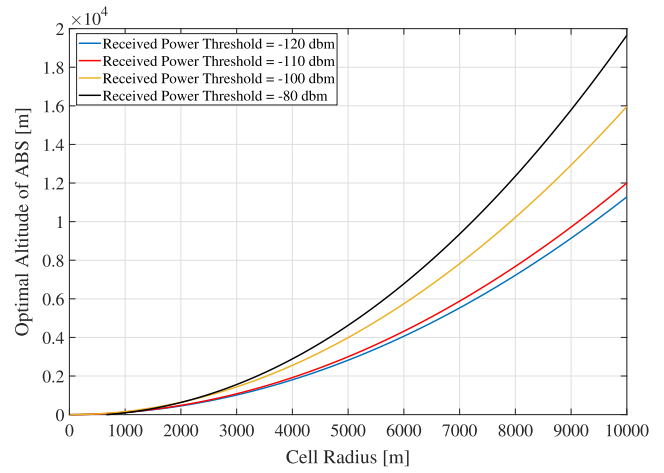(a) Suburban Environment at ABS altitude of 600 m
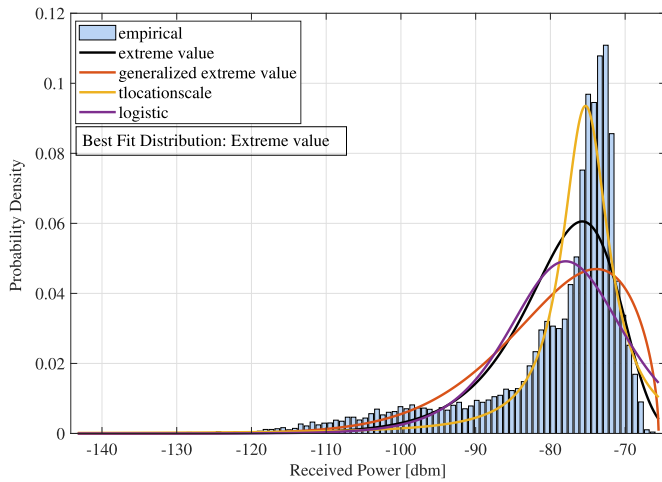
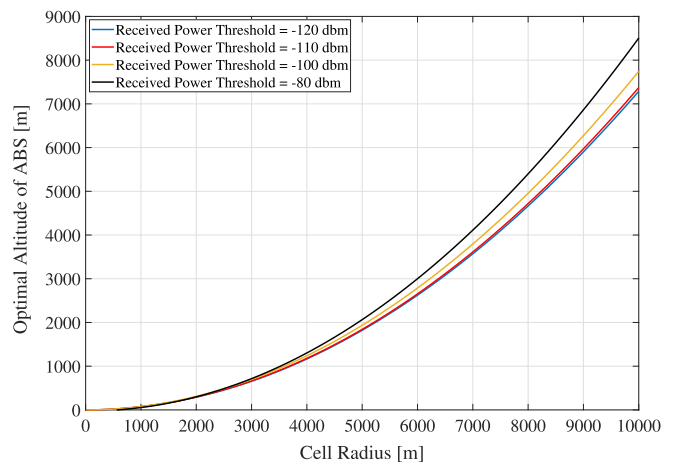(b) Urban Environment at ABS altitude of 400 m
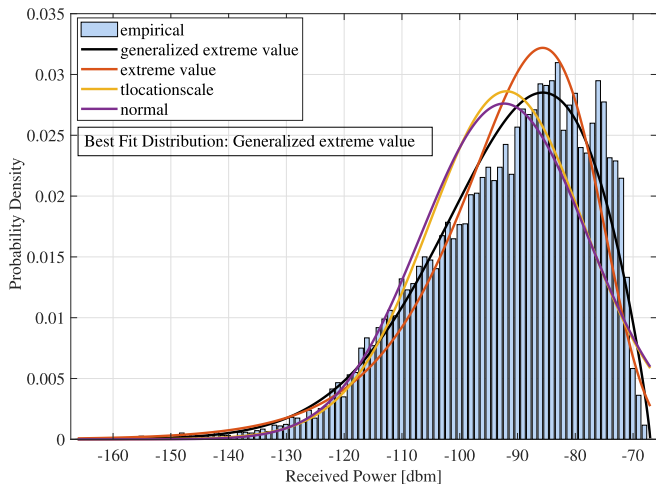
(c) Urban High Rise Environment at ABS altitude of 600 m

Fig. 6. Received power distribution of ground receivers in different environments at optimal ABS altitude. (a) [Suburban Environment at ABS altitude of 600 m]. (b) [Urban Environment at ABS altitude of 400 m]. (c) [Urban High Rise Environment at ABS altitude of 600 m].
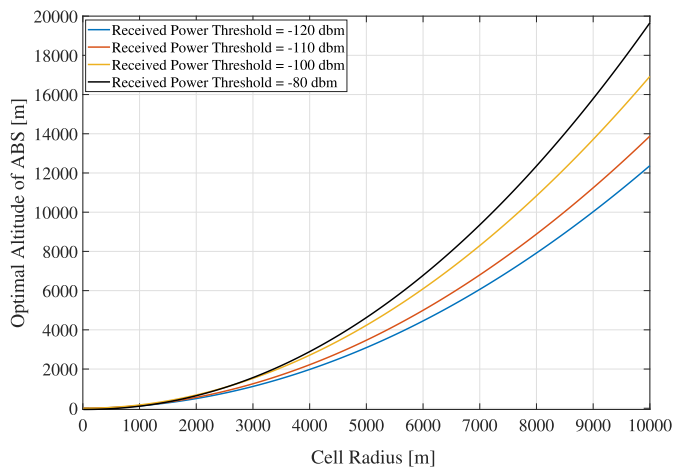
Therefore, even with complex trajectories, similar channel measurements and SER results are expected.

(a) Suburban environment.

(b) Urban environment.

(c) Urban High Rise environment.

Fig. 7. Optimal ABS altitude variation with cell radius. (a) [Suburban environment.] (b) [Urban environment.] (c) [Urban High Rise environment.]

It is possible to obtain the OFDM waveform from the GFDM one, by setting the number of sub-carriers to $K = 64$ and the number of sub-symbols to $M = 1$ with Dirichlet pulse shaping filter. We have performed simulations with static and
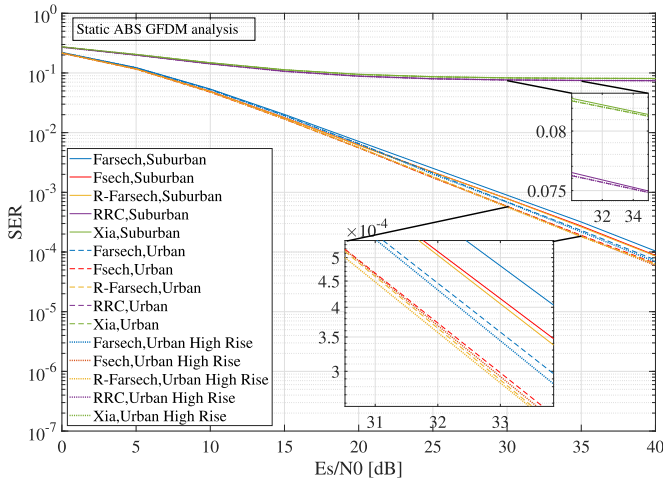
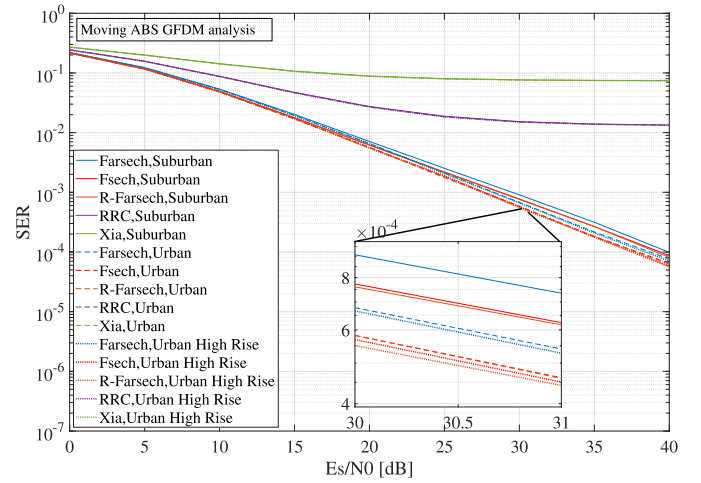Fig. 8.   GFDM SER analysis for static ABS.

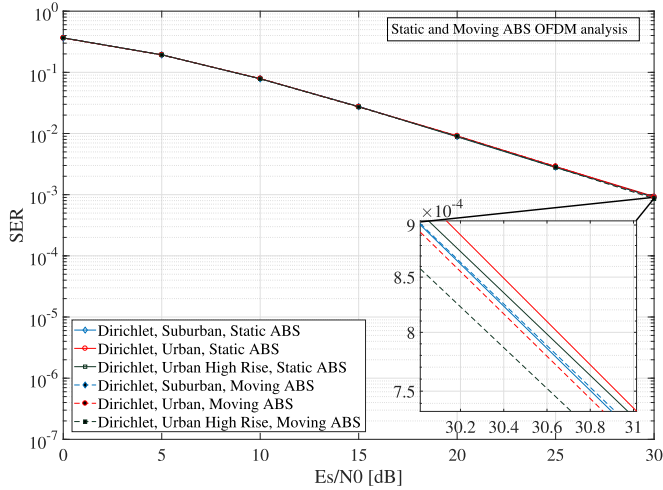Fig. 10.   GFDM SER analysis for moving ABS.

Fig. 9.   OFDM SER analysis for static and moving ABS.

moving ABS with the same maximum Doppler shift considered in GFDM system, as shown in Fig. 9. The simulation parameters were taken from [22], considering the maximum relative movement between the ABS and user. We observe that a similar behavior was obtained as reported in [22] with certain deviation since we use realistic A2G channel parameters obtained from ray tracing. This also provides insight to the validation of our OFDM and GFDM simulations. It is also significant to scrutinize that Wi-Fi also operates at 2.4 GHz carrier frequency. However, Wi-Fi based PHY is challenging to provide reliability in vehicular communication [35]. Also, as shown in [35], GFDM performs better than OFDM with Wi-Fi parameters due to higher throughput and better spectral and temporal characteristics. This implies GFDM has a better performance than OFDM at 2.4 GHz band.

To summarize, we enhance the performance of ABS downlink communication system by addressing its optimal altitude for maximum coverage and minimum SER with implementation of GFDM waveform and BTN pulse shaping filters. Our solution can be implemented in real-time,

where mobile operators can deploy ABS network, either as independent ABSs or to support the terrestrial network, with defined altitudes, waveforms, and suitable pulse-shaping to optimize the performance based on different data requirements of ground users. The main advantage is the possibility of relaying on closed-form expressions of ABS cellular coverage, BTN pulse-shaping filters, GFDM transmission scheme with simulation and channel parameters.

VII. CONCLUSION AND FUTURE WORK

In this article, we have shown the Symbol Error Rate (SER) analysis of LTE-Compatible GFDM, under low-latency scenario with GFDM symbol duration of 66.67 μs and "Better than Nyquist" pulse shaping filters for a static and moving Aerial Base Station (ABS) providing cellular connectivity to ground users. We also address the SER results for OFDM. We have performed these simulations in different generalized environments- Suburban, Urban, and Urban High Rise, developed according to ITU-R parameters, at optimal altitude of ABS. The optimal altitude was defined based on two criterion's'- maximum cell coverage and minimum SER. Also, Air-to-Ground channel parameters were used to obtain SER simulation results, obtained from ray tracing results on a commercial radio propagation software. The power delay profile and probability distribution parameters of received power were also provided at the optimal altitude to reproduce the entire set of results without redoing the whole stack of operations. This also supplemented to show the variation of optimal altitude with cell area. For future works, we resort to hardware implementation for quantitative analysis to generate proof of concepts for algorithms implemented in this article. We also realise the importance to include other possible tradeoffs and their dependency on metrics such as energy efficiency, millimeter wave transmission, and directional antenna models to define a more complex optimization problem to find the ABS optimal altitude. Further, we plan to evaluate the

features of other waveforms such as Universal Filtered Multi-Carrier (UFMC) and Filter Bank Multi-carrier (FBMC) modulations for various UAV use-case scenarios in heterogeneous network.

ACKNOWLEDGMENT

REFERENCES

[1] N. Sharma, A. Kumar, M. Magarini, S. Bregni, and D. N. K. Jayakody, "Impact of CFO on low latency-enabled UAV using 'better than nyquist' pulse shaping in GFDM," in *Proc. IEEE 89th Veh. Technol. Conf.*, Apr. 2019, pp. 1–6.

[2] S. Chandrasekharan *et al.*, "Designing and implementing future aerial communication networks," *IEEE Commun. Mag.*, vol. 54, no. 5, pp. 26–34, May 2016.

[3] S. Hayat, E. Yanmaz, and R. Muzaffar, "Survey on unmanned aerial vehicle networks for civil applications: A communications viewpoint," *IEEE Commun. Surv. Tut.*, vol. 18, no. 4, pp. 2624–2661, Oct.–Dec. 2016.

[4] R. Gupta, A. Kumari, S. Tanwar, and N. Kumar, "Blockchain-envisioned softwarized multi-swarming UAVs to tackle COVID-I9 situations," *IEEE Netw.*, vol. 35, no. 2, pp. 160–167, Mar./Apr. 2021.

[5] A. Fotouhi *et al.*, "Survey on UAV cellular communications: Practical aspects, standardization advancements, regulation, and security challenges," *IEEE Commun. Surv. Tut.*, vol. 21, no. 4, pp. 3417–3442, Oct.–Dec. 2019.

[6] X. Wang, H. Zhang, Y. Tian, and V. C. M. Leung, "Modeling and analysis of aerial base station-assisted cellular networks in finite areas under LoS and NLoS propagation," *IEEE Trans. Wireless Commun.*, vol. 17, no. 10, pp. 6985–7000, Oct. 2018.

[7] 3GPP. "Technical specification group radio access network; enhancement for unmanned aerial vehicles; Stage 1 (Release 17)," Tech. Rep. 22.829, Sep. 2019.

[8] Y. Zeng, R. Zhang, and T. J. Lim, "Wireless communications with unmanned aerial vehicles: Opportunities and challenges," *IEEE Commun. Mag.*, vol. 54, no. 5, pp. 36–42, May 2016.

[9] B. Bera, S. Saha, A. K. Das, N. Kumar, P. Lorenz, and M. Alazab, "Blockchain-envisioned secure data delivery and collection scheme for 5G-based IoT-enabled internet of drones environment," *IEEE Trans. Veh. Technol.*, vol. 69, no. 8, pp. 9097–9111, Aug. 2020.

[10] A. A. Khuwaja, Y. Chen, N. Zhao, M. Alouini, and P. Dobbins, "A survey of channel modeling for UAV communications," *IEEE Commun. Surv. Tut.*, vol. 20, no. 4, pp. 2804–2821, Oct.–Dec. 2018.

[11] C. Yan, L. Fu, J. Zhang, and J. Wang, "A comprehensive survey on UAV communication channel modeling," *IEEE Access*, vol. 7, pp. 107769–107792, Aug. 2019, doi: 10.1109/ACCESS.2019.2933173.

[12] W. Khawaja, I. Guvenc, D. W. Matolak, U. Fiebig, and N. Schneckenburger, "A survey of air-to-ground propagation channel modeling for unmanned aerial vehicles," *IEEE Commun. Surv. Tut.*, vol. 21, no. 3, pp. 2361–2391, Jul./Sep. 2019.

[13] N. Sharma, M. Magarini, L. Dossi, L. Reggiani, and R. Nebuloni, "A study of channel model parameters for aerial base stations at 2.4 GHz in different environments," in *Proc. 15th IEEE Annu. Consum. Commun. Netw. Conf.*, Jan. 2018, pp. 1–6.

[14] R. Zhang, Q. Guo, D. Zhai, D. Zhou, X. Du, and M. Guizani, "Channel measurement and resource allocation scheme for dual-band airborne access networks," *IEEE Access*, vol. 7, pp. 80870–80883, 2019.

[15] Z. Cui *et al.*, "Low-altitude UAV air-ground propagation channel measurement and analysis in a suburban environment at 3.9 GHz," *IET Microw., Antennas Propag.*, vol. 13, no. 9, pp. 1503–1508, 2019.

[16] A. Al-Hourani, S. Kandeepan, and S. Lardner, "Optimal LAP altitude for maximum coverage," *IEEE Wireless Commun. Lett.*, vol. 3, no. 6, pp. 569–572, Dec. 2014.

[17] M. M. Azari, F. Rosas, K. Chen, and S. Pollin, "Ultra reliable UAV communication using altitude and cooperation diversity," *IEEE Trans. Commun.*, vol. 66, no. 1, pp. 330–344, Jan. 2018.

[18] H. He, S. Zhang, Y. Zeng, and R. Zhang, "Joint altitude and beamwidth optimization for UAV-enabled multiuser communications," *IEEE Commun. Lett.*, vol. 22, no. 2, pp. 344–347, Feb. 2018.

[19] W. Huang, D. M. Kim, W. Ding, and P. Popovski, "Joint optimization of altitude and transmission direction in UAV-based two-way communication," *IEEE Wireless Commun. Lett.*, vol. 8, no. 4, pp. 984–987, Aug. 2019.

[20] K. Lim, H. Kim, T. C. Hong, and J. Y. Ahn, "Wideband channel waveform and structure for unmanned aircraft systems," in *Proc. Int. Conf. Inform. Commun. Technol. Convergence*, Oct. 2017, pp. 1222–1224.

[21] J. Kakar and V. Marojevic, "Waveform and spectrum management for unmanned aerial systems beyond 2025," in *Proc. IEEE 28th Annu. Int. Symp. Pers., Indoor, Mobile Radio Commun.*, Oct. 2017, pp. 1–5.

[22] Z. Wu, H. Kumar, and A. Davari, "Performance evaluation of OFDM transmission in UAV wireless communication," in *Proc. 37th Southeastern Symp. Syst. Theory, 2005*, Mar. 2005, pp. 6–10.

[23] M. Jacovic, O. Bshara, and K. R. Dandekar, "Waveform design of UAV data links in urban environments for interference mitigation," in *Proc. IEEE 88th Veh. Technol. Conf.*, Aug. 2018, pp. 1–5.

[24] C. Blümm, C. Heller, and R. Weigel, "SDR OFDM waveform design for a UGV/UAV communication scenario," *J. Signal Process. Syst.*, vol. 69, no. 1, pp. 11–21, 2012.

[25] Y. Yang, L. Zhu, X. Mao, Q. Tan, and Z. He, "The spread spectrum GFDM schemes for integrated satellite-terrestrial communication system," *China Commun.*, vol. 16, no. 12, pp. 165–175, 2019.

[26] M. Murad, I. A. Tasadduq, and P. Otero, "Towards multicarrier waveforms beyond OFDM: Performance analysis of GFDM modulation for underwater acoustic channels," *IEEE Access*, vol. 8, pp. 222782–222799, Dec. 2020, doi: 10.1109/ACCESS.2020.3043718.

[27] K. Vejandla, S. P. Valluri, V. M. Vakamulla, M. Sellathurai, A. Kumar, and T. Ratnarajah, "Performance analysis under double sided clipping and real time implementation of DCO-GFDM in VLC systems," *J. Lightw. Technol.*, vol. 39, no. 1, pp. 33–41, Jan. 2021, doi: 10.1109/JLT.2020.3026381.

[28] Z. Na, J. Lv, F. Jiang, M. Xiong, and N. Zhao, "Joint subcarrier and sub-symbol allocation-based simultaneous wireless information and power transfer for multiuser GFDM in IoT," *IEEE Internet Things J.*, vol. 6, no. 4, pp. 5999–6006, Aug. 2019.

[29] Qualcomm, "Cellular drone communication." Accessed: Mar. 13, 2021. [Online]. Available: https://www.qualcomm.com/research/technologies/lte/advanced-pro/cellular-drone-communication

[30] Facebook, "Technology behind aquila." Accessed: Mar. 13, 2021. [Online]. Available: https://www.unifly.aero/news/global-internet-access-with-facebook-aquila

[31] Nokia, "Drone networks." Accessed: Mar. 13, 2021. [Online]. Available: https://dac.nokia.com/applications/nokia-drone-networks/#about

[32] I. Gaspar, L. Mendes, M. Matthé, N. Michailow, A. Festag, and G. Fettweis, "LTE-compatible 5G PHY based on generalized frequency division multiplexing," in *Proc. 11th Int. Symp. Wireless Commun. Syst.*, Aug. 2014, pp. 209–213.

[33] R. Blasco, H. Do, S. Shalmashi, S. Sorrentino, and Y. Zang, "3GPP LTE enhancements for V2V and comparison to IEEE 802.11 P," in *Proc. 11th ITS Eur. Congr.*, 2016, pp. 6–9.

[34] A. Festag, "Cooperative intelligent transport systems standards in Europe," *IEEE Commun. Mag.*, vol. 52, no. 12, pp. 166–172, Dec. 2014.

[35] D. Zhang, A. Festag, and G. P. Fettweis, "Performance of generalized frequency division multiplexing based physical layer in vehicular communications," *IEEE Trans. Veh. Technol.*, vol. 66, no. 11, pp. 9809–9824, Nov. 2017.

[36] N. Michailow *et al.*, "Generalized frequency division multiplexing for 5th generation cellular networks," *IEEE Trans. Commun.*, vol. 62, no. 9, pp. 3045–3061, Sep. 2014.

[37] W. Khawaja, I. Guvenc, D. W. Matolak, U. Fiebig, and N. Schneckenberger, "A survey of air-to-ground propagation channel modeling for unmanned aerial vehicles," *IEEE Commun. Surv. Tut.*, vol. 21, no. 3, pp. 2361–2391, May. 2019, doi: 10.1109/COMST.2019.2915069.

[38] A. Kumar, M. Magarini, and S. Bregni, "Impact of better than nyquist pulse shaping in GFDM PHY with LTE-compatible frame structure," in *Proc. IEEE 9th Latin-Amer. Conf. Commun.*, Nov. 2017, pp. 1–6.

[39] A. Kumar and M. Magarini, "Improved nyquist pulse shaping filters for generalized frequency division multiplexing," in *Proc. 8th IEEE Latin-Amer. Conf. Commun.*, Nov. 2016, pp. 1–7.

[40] "Propagation data and prediction methods for the design of terrestrial broadband millimetric radio access systems operating in a frequency range from 3 to 60 GHz," Radiowave Propagation, Geneva, Switzerland, Rec. P.1410-5, Feb. 2012.

[41] Wireless insite, 3D wireless prediction software." Accessed: Mar. 13, 2021. [Online]. Available: https://www.remcom.com/wireless-insite-em-propagation-software/

[42] P. Medeović, M. Veletić, and Ž. Blagojević, "Wireless insite software verification via analysis and comparison of simulation and measurement results," in *Proc. 35th Int. Conv.*, 2012, pp. 776–781.

[43] D. G. Cileo, N. Sharma, and M. Magarini, "Coverage, capacity and interference analysis for an aerial base station in different environments," in *Proc. Int. Symp. Wireless Commun. Syst.*, Aug. 2017, pp. 281–286.

[44] S. Sun *et al.*, "Propagation path loss models for 5G urban micro- and macro-cellular scenarios," in *Proc. IEEE 83rd Veh. Technol. Conf.*, May 2016, pp. 1–6.

[45] "Solid angle" from mathWorld-A Wolfram web resource. Accessed: Mar. 13, 2021. [Online]. Available: http://mathworld.wolfram.com/SolidAngle.html

[46] C. C. Tan and N. C. Beaulieu, "An investigation of transmission properties of xia pulses," in *Proc. IEEE Int. Conf. Commun.*, 1999, vol. 2, pp. 1197–1201.

Navuday Sharma received the M.Tech. degree in avionics engineering from the Institute of Space Science and Technology, Amity University, Noida, India, in 2015 and the Ph.D. degree in telecommunication engineering from the Department of Electronics, Information and Bio-engineering , Politecnico di Milano, Milan, Italy, in 2018. From October 2017 to June 2018, he was also a Research Engineer with the Infocomm Lab, School of Computer Science and Robotics, Tomsk Polytechnic University, Tomsk, Russia.. From October 2018 to February 2020, he was a Postdoctoral Researcher with the Thomas Johann Seebeck Department of Electronics, Tallinn University of Technology, Tallinn, Estonia.. He is currently a RF Test Development Engineer with Ericsson Estonia. He has worked on wireless communication with aerial base stations for 5G systems and is currently working toward ultra-reliable low latency communication. His other research interests include channel modeling, multi-carrier communication, digital signal processing, and Internet of Things.

Atul Kumar received the B.Tech. degree in electronics and communication engineering, in 2013, the M. S. degree in electronics engineering in September 2015, and Ph.D. degree in information engineering from the Dipartimento di Elettronica, Informazione and Bioingegneria in December 2018 from the Politecnico di Milano, Milan, Italy. Since December 2018, he has been a Research Associate with Vodafone Chair Mobile Communications Systems, Technische Universität Dresden, Dresden, Germany. His main research interests include wireless cellular systems, synchronization errors, LTE-A Physical layers, new radio, beam forming, massive multiple-input and multiple-output, orthogonal frequency division multiplexing, generalized frequency division multiplexing, and non-orthogonal multiple access.

Haris Pervaiz received the M.Sc. degree in information security from the Royal Holloway, University of London, Egham, U.K., in 2005, and the Ph.D. degree from the School of Computing and Communication, Lancaster University, Lancaster, U.K. He is currently a Lecturer with InfoLab21, Lancaster University. From 2017 to 2018, he was a Research Fellow with the 5G Innovation Centre, University of Surrey, Guildford, U.K. and from 2016 to 2017, an EPSRC Doctoral Prize Fellow with the School of Computing and Communication, Lancaster University. His current research interests include green heterogeneous wireless communications and networking, 5G and beyond, millimeter wave communication, and energy and spectral efficiency. He has been actively involved in projects, such as CROWN, CogGREEN, TWEETHER, and Energy Proportional EnodeB for LTE-Advanced and Beyond and the DARE project, and an ESPRC funded project. He is an Associate Editor for the IEEE ACCESS, an Editorial Board Member of the *Emerging Telecommunications Technologies* (Wiley), and an Associate Editor for the *Internet Technology Letters* (Wiley).

Maurizio Magarini received the M.Sc. and Ph.D. degrees in electronic engineering from the Politecnico di Milano, Milan, Italy, in 1994 and 1999, respectively. From 1999 to 2001, he was a Research Associate with the Dipartimento di Elettronica, Informazione e Bioingegneria, Politecnico di Milano . From 2001 to 2018, he was an Assistant Professor with Politecnico di Milano where, since June 2018, he has been an Associate Professor. From August 2008 to January 2009, he spent a sabbatical leave with Bell Labs, Alcatel-Lucent, Holmdel, NJ, USA. He has authored and coauthored more than 100 journal and conference papers. His research interests include the broad area of communication and information theory including synchronization, channel estimation, and equalization and coding applied to wireless and optical communication systems. His most recent research activities have focused on molecular communications, massive MIMO, study of waveforms for 5G cellular systems, vehicular communications, wireless sensor networks for mission critical applications, and wireless networks using unmanned aerial vehicles and high-altitude platforms. In 1994, he was the recipient of the TELECOM Italia scholarship award for his M.Sc. Thesis. He was the co-recipient of two best paper awards. He is an Associate Editor for IEEE ACCESS, *IET Electronics Letters*, and *Nano Communication Networks* (Elsevier). He has been involved in several European and National research projects.

Leila Musavian received the Ph.D. degree in telecommunications from Kings College London, London, U.K. She is currently a Professor of wireless communications with the University of Essex, Colchester, U.K. From September 2018 to December 2020, she was the Deputy Pro-Vice-Chancellor for Research with the University of Essex and from December 2016 to October 2020, a Reader in telecommunications with the School of Computer Science and Electronic Engineering. From December 2012 to August 2016 and August 2016 to November 2016, she was a Lecturer and then a Senior Lecturer with InfoLab21, Lancaster University, Lancaster, U.K. From 2011 to 2012, she was a Research Associate with McGill University, Montreal, QC, Canada. From 2009 to 2010, she was a Research Associate with Loughborough University, Loughborough, U.K., and from 2006 to 2008, a Postdoctoral Fellow with INRS-EMT, Montreal, QC, Canada. Her research interests include radio resource management for 6G/B5G communications, low latency communications, machine learning for communications, mmWave communications, massive MIMO, and energy harvesting communications. From 2015 to 2020, she was the editor of IEEE TRANSACTIONS OF WIRELESS COMMUNICATIONS. From 2016 to 2019, she was the Executive Editor of *Transactions on Emerging Telecommunications Technologies* and an Associate Editor for Wiley *Internet Technology Letters*. She has been the Lead Chair for UHS5G WP in the IEEE Globecom 2018, UHSLLS WP in the IEEE WCNC 2019, Lead Chair for URLLC Special Session in the IEEE PIMRC 2018, the TPC Co-Chair of CorNer 2016 (in conjunction with ISWCS 2016) and the Co-Chair of mmWave 5G (STEMCOM 2016) and also a TPC Member of several conferences including the IEEE ICC, the IEEE GLOBECOM, the IEEE WCNC, the IEEE ICCCN, the IEEE PIMRC, and the ChinaCom. She was the workshop Co-Chair of the VTC-Spring-2020 and is currently the Wireless Communications Symposium Lead Co-Chair for the IEEE ICC 2021, in Montreal, QC, Canada.

Muhamamd Mahtab Alam (Senior Member, IEEE) received the M.Sc. degree in electrical engineering from Aalborg University, Aalborg, Denmark, in 2007, and the Ph.D. degree in signal processing and telecommunication from the University of Rennes 1 (INRIA Research Center), Rennes, France, in 2013. In 2013, he was an Assistant Professor with the Swedish College of Engineering and Technology, Rawalpindi, Pakistan. From 2014 to 2016, he did his Postdoc research with Qatar Mobility Innovation Center, Doha, Qatar. In 2016, he was the European Research Area Chair and an Associate Professor with the Thomas Johann Seebeck Department of Electronics, Tallinn University of Technology, Tallinn, Estonia, where later in 2018, he was elected as a Professor. From 2019, he is the communication systems research group leader. He has the authored and coauthored more than 85 research publications. His research interests include wireless communications - connectivity, NB-IoT 5G/B5G services and applications, and low-power wearable networks for SmartHealth. He hasmore than 15 years of combined academic and industrial multinational experiences while working in Denmark, Belgium, France, Qatar and Estonia. He has several leading roles as PI in multimillion Euros international projects funded by European Commission (H2020-ICT-2019-3, "951867", NATO-SPS (G5482), Estonian Research Council (PRG424), and Telia industrial grant.

Muhammad Ali Imran (Senior Member, IEEE) is a Fellow IET, Senior Fellow HEA is Dean University of Glasgow UESTC and a Professor of wireless communication systems with research interests in self organised networks, wireless networked control systems and the wireless sensor systems. He heads the Communications, Sensing and Imaging (CSI) research group with University of Glasgow and is the Director of Centre for Educational Development and Innovation. He is an Affiliate Professor with the University of Oklahoma, USA and a Visiting Professor with 5G Innovation Centre, University of Surrey, U.K. He has more than 20 years of combined academic and industry experience with several leading roles in multi-million pounds funded projects. He has filed 15 patents, he has authored or coauthored more than 400 journal and conference publications, has authored two books, edited eight books and authored more than 30 book chapters, has successfully supervised more than 40 postgraduate students at Doctoral level. He has been a consultant to international projects and local companies in the area of self-organised networks.

Anish Jindal (Senior Member, IEEE) received the B. Tech, M.E., and Ph.D. degrees in computer science engineering in 2012, 2014, and 2018, respectively. Since March 2020, he has been a Lecturer with the School of Computer Science and Electronic Engineering, University of Essex, Colchester, U.K. From October 2018 to March 2020, he was a Senior Research Associate with the School of Computing & Communications, Lancaster University, Lancaster, U.K. He is the Guest Editor of various journals including the *Software: Practice and Experience* (Wiley) and *Computers* (MDPI). His research interests include smart cities, data analytics, artificial intelligence, cyber-physical systems, wireless networks, and security. He was the recipient of the Outstanding Ph.D. Dissertation Award, 2019 from the IEEE Technical Committee on Scalable Computing (TCSC) and the IEEE Communication Society's Outstanding Young Researcher Award for the Europe, Middle East, and Africa (EMEA) Region, 2019. He was the General Co-Chair, the TPC Co-Chair, a TPC Member, the Publicity Chair and the Session Chair of various reputed conferences and workshops including the IEEE ICC, the IEEE WoWMoM, the IEEE INFOCOM and the IEEE GLOBECOM. He is actively involved with various working groups and committees of IEEE and ACM related to smart grid, energy informatics, and smart cities.